J. Fluid Mech. (1999), *vol.* 383, *pp.* 353–378. Printed in the United Kingdom

© 1999 Cambridge University Press

Flow through a charged biopolymer layer

By A. J. MOKADY[1,2], A. J. MESTEL[1] AND C. P. WINLOVE[2]

[1]Mathematics Department, Imperial College, 180 Queen's Gate, London SW7 2BZ, UK

[2]Centre for Biological and Medical Systems, Imperial College, London SW7 2AZ, UK

(Received 25 September 1997 and in revised form 4 November 1998)

The polyelectrolyte layer coating mammalian cells, known as the glycocalyx, is important in communicating flow information to the cell. In this paper, the layer is modelled as a semi-infinite, doubly periodic array of parallel charged cylinders. The electric potential and ion distributions surrounding such an array are found using the Poisson–Boltzmann equation and an iterative domain decomposition technique. Similar methods are used to calculate Stokes flows, driven either by a shear at infinity or by an electric field, parallel or transverse to the cylinders. The resulting electric streaming currents due to flow over endothelial cells, and the electrophoretic mobilities of red blood cells are deduced as functions of polymer concentration and electrolyte molarity. It is shown that only the top portion of the layer is important in these effects.

1. Introduction

The surfaces of mammalian cells are coated with a layer of highly charged polymer molecules which, on some cells, may be up to 1 μm thick. This layer is known as the glycocalyx, which literally means 'sugar coat'. It was first described by Luft (1965) who observed a 'fluffy' layer on endothelial cells taken from capillaries. Since then, it has been studied most extensively on erythrocytes (red blood cells). Figure 1 shows an electron micrograph of the glycocalyx on a vascular endothelial cell.

As the glycocalyx forms the outermost cell layer, it can be expected to influence transport into and out of the cell, and interactions between cells. For example, electrostatic repulsion between the glycocalyx layers on different cells might inhibit cohesion between cells. Such an effect is of particular relevance to the flow of blood through capillaries, when the glycocalyces of the erythrocytes and endothelial cells lining the vessels are in close proximity. There is evidence that this regulates blood flow through the vessels (Desjardins & Duling 1990).

More generally, the glycocalyx acts as a flow transducer to convey information about blood flow to the endothelial cells, which then respond accordingly. The detailed mechanism of this process, including the role of the glycocalyx, is not yet understood, but it is known that advection of the ions surrounding the glycocalyx generates electric streaming potentials which may convey information to the cell. Likewise, the glycocalyx experiences a force due to flow above it, which is transmitted to the cell membrane beneath. A general review of mechano-transduction in endothelial cells is given by Davies (1995).

Electrical effects are also important in electrophoresis experiments, in which the motion of red blood cells in an imposed electric field is studied. The charged surface

https://doi.org/10.1017/S0022112098004030 Published online by Cambridge University Press

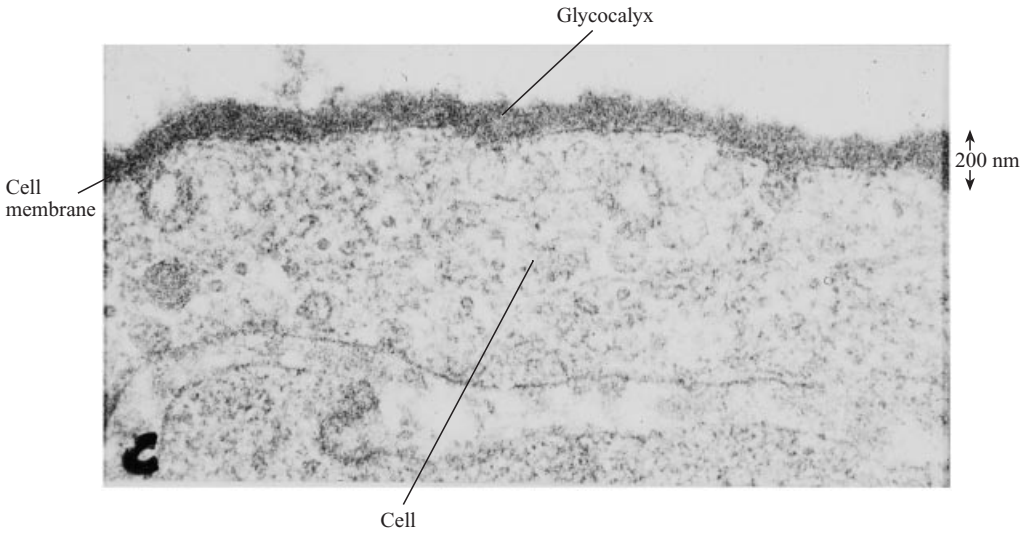


FIGURE 1. The endothelial glycocalyx of the rabbit carotid artery stained with 0.2% Alcian blue in 0.3 M $MgCl_2$.

of red blood cells changes under pathological conditions and their electrochemical properties have been much studied in this manner (Seaman 1983).

The aim of the present work is to develop a formalism applicable both to the migration of red cells in an electric field and to the generation of electric currents and potentials by flow over the endothelial cell surface. It is necessary to consider not only the hydrodynamic effects of the surface molecules, which effectively form a porous medium, but also their electrical interactions with mobile ions. Some aspects of the problem have been considered in other contexts involving unbounded polyelectrolyte media or bounded but uncharged porous media.

Polyelectrolyte molecules have large molecular weight and become ionized in contact with water, when their associated counter-ions become free hydrated ions in the surrounding solution. In equilibrium, these counter-ions together with any other ions present surround an isolated, charged molecule forming an electrical double layer. The characteristic thickness of this layer, known as the Debye length, depends on the charge density of the polyelectrolyte and the ionic strength of the surrounding solution of mobile ions. As fluid moves through the layer it advects ions, generating a streaming current which is detected by the streaming potential gradient it induces. This process occurs in all blood vessels, although in practice, streaming potentials are difficult to measure *in vivo* except in the large vessels such as the aorta (Sawyer & Srinivasan 1972).

When the electrical double layers are thin various models are possible. For example, Edwards (1995) considered pressure-driven flows through an unbounded porous medium. In the glycocalyx, however, the flow is driven by shear above the layer and, furthermore, adjacent macromolecules interact electrically as the separation distance is comparable to the Debye length. The standard model for calculating ion distributions is to treat individual polyelectrolyte molecules as infinitely long circular cylinders, with a uniform surface charge density. The reasoning behind this is that the high charge density of the polyelectrolytes will cause adjacent polymer segments to repel each other, so that the molecule adopts a much more stretched configuration than would

https://doi.org/10.1017/S0022112098004030 Published online by Cambridge University Press

an uncharged polymer of similar structure. The distribution of ions surrounding the molecule is then found using the Poisson–Boltzmann equation (see § 2). The effect of an array of polyelectrolyte molecules can be incorporated into the model by using a 'cylindrical cell' approximation in which the presence of the other macromolecules in the system is represented by imposing a suitable boundary condition on a cylindrical outer boundary (Kuhn, Kunzle & Katchalsky 1948; Katchalsky 1971). This approach has been used more recently to model the polyelectrolyte properties of biological tissues by several researchers (e.g. Phillips 1987; Edwards 1995). Similar cylindrical cell approximations were used for the Stokes equations by Happel (1957, 1958, 1959).

Other researchers have represented the geometry of regular arrays of cylinders more accurately. Sparrow & Loeffler (1959) solved the Stokes equations numerically for axial flow past square and triangular arrays of cylinders. The solutions were expressed as Fourier series in polar coordinates, with the coefficients being found by sampling boundary value points and solving the resulting linear least-squares problem numerically. A similar method was used by Sangani & Acrivos (1982) for flow perpendicular to the cylinders for square and hexagonal arrays. Drummond & Tahir (1984) calculated both the axial and transverse flow for square, triangular, hexagonal and rectangular arrays of cylinders using a Stokeslet method. These papers were compared with experimental data by Jackson & James (1986) who found generally good agreement between the theoretical approaches and between the theory and experimental measurements.

The above works have assumed an unbounded array of molecules. The glycocalyx however has an upper boundary and, furthermore, the interactions between the polymer layer and the pure fluid are important. We shall find that some of the measurable quantitities are determined only by the top of the glycocalyx, rather than its deep interior. In this paper we shall consider a semi-infinite layer of regularly spaced cylinders, on the lines of Larson & Higdon (1986, 1987). We extend their results to include electrical effects.

We model the glycocalyx as a semi-infinite square array of infinite circular cylinders, parallel to the cell surface, with a uniform surface charge density, as shown in figure 2. In treating the glycocalyx in this way, it is assumed that there are no substantial gaps between neighbouring polymer chains and that these chains are aligned along the z-axis. This latter assumption is questionable. However, if the full flow is regarded as a suitable superposition of components parallel and transverse to the cylinders, the results should be appropriate.

The content of this paper is as follows: In § 2 we calculate the ionic distributions and electric potential for semi-infinite arrays of uniformly charged cylinders, using an iterative, domain-decomposition method. In § 3 we examine axial Stokes flows parallel to the cylinders driven either by a shear or by an imposed electric field. The resulting streaming currents and electrophoretic velocities are calculated. In § 4 the corresponding results for flows transverse to the direction of the cylinders are derived. The implications and limitations of the model are discussed in § 5. A more detailed account of the physiological relevance and applications will be presented elsewhere (Mestel *et al.* 1999).

2. The electric potential

The electric potential, Φ, satisfies a Poisson equation

$$\nabla^2 \Phi = -\frac{\rho}{\varepsilon}, \tag{2.1}$$

https://doi.org/10.1017/S0022112098004030 Published online by Cambridge University Press

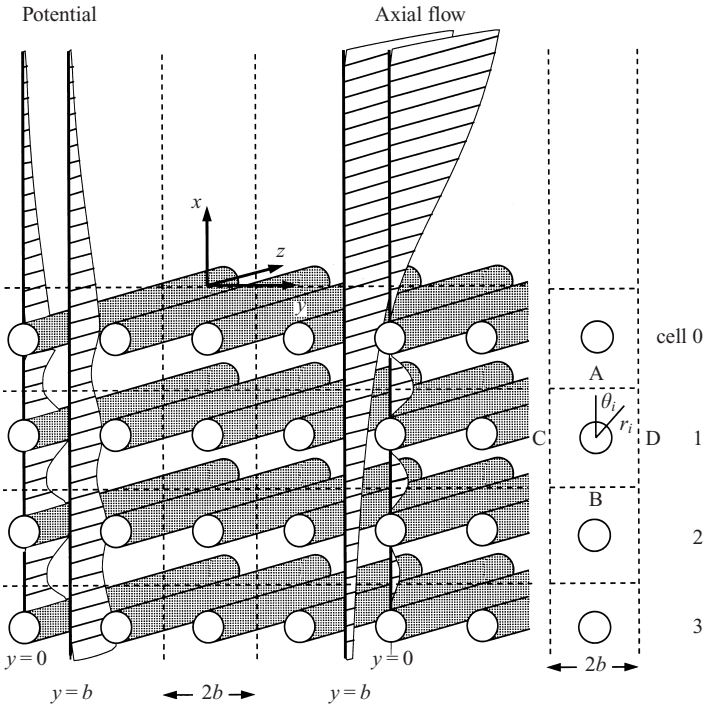


FIGURE 2. A semi-infinite, doubly-periodic array of charged cylinders. Schematic representations of the potential (left) and shear-driven axial flow (middle) are drawn midway between cylinders ($y = b$) and passing through the cylinders ($y = 0$). The potential decays exponentially with the Debye length in $x > 0$, and soon becomes periodic as $x \to -\infty$. The velocity becomes self-similar in $x < 0$, decaying with a scale factor from cylinder to cylinder. In the iterative scheme boundary conditions from $x = \pm\infty$ are passed up and down between squares (right).

where ε is the electric permittivity of the solution. The permittivity may vary a little with the ion concentrations, but we will take it to be constant. The charge density, ρ, due to I distinct ion species is assumed to satisfy a Boltzmann distribution

$$\rho(\Phi) = \sum_{i=1}^{I} e z_i n_i^0 \exp\left(-\frac{e z_i}{kT}\Phi\right), \tag{2.2}$$

where $-e$ is the charge of an electron, k is the Boltzmann constant, T is the absolute temperature, while n_i^0 is the concentration of ion type i in the fluid far from the glycocalyx and z_i its valency. In physiological conditions, the most common ions present are sodium (Na^+), chloride (Cl^-) and an order of magnitude lower concentration of calcium (Ca^{2+}). Electrical neutrality at infinity requires $\sum z_i n_i^0 = 0$, so that, neglecting the calcium ions, there are equal concentrations of sodium and chloride ions at infinity.

The Poisson–Boltzmann equation (2.1) with (2.2) may be linearized provided the electrical potential $\Phi \ll kT/e$ to obtain

$$\nabla^2\Phi = \kappa^2\Phi \tag{2.3}$$

where κ^{-1} is the Debye length, given in terms of the above parameters by

$$\kappa^2 = \frac{e^2}{\varepsilon k T}\sum_{i=1}^{I} z_i^2 n_i^0. \tag{2.4}$$

https://doi.org/10.1017/S0022112098004030 Published online by Cambridge University Press

A long polyelectrolyte molecule will be modelled as an infinite rigid cylinder of radius a on whose surface the condition

$$\frac{\partial \Phi}{\partial r} = -\frac{Q}{\varepsilon} \tag{2.5}$$

is imposed. By Gauss' law, this corresponds to a total charge $2\pi aQ$ per unit axial length on the cylinder. It is simplest to think of Q as being a uniform surface charge density, although formally this is so only if the surface tangential field is small or if the cylinder interior has relatively low permittivity. In practice, the radially symmetric part of Φ is indeed dominant near $r = 1$ and so it would be reasonable to treat Q as a surface charge. Instead, we will regard the charge as being suitably distributed over the cylinder cross-section. The cylinder interior will be assumed to have the same electrical properties as the surrounding fluid, so that when in § 3 and § 4 we consider electrophoresis and superimpose an external field on the system, this field is unaltered by the presence of the cylinders. This need not be the case in other models (Derjaguin & Dukhin 1974).

We non-dimensionalize using the length scale a writing

$$\phi = -\frac{e}{kT}\Phi, \quad \sigma = \frac{Qea}{\varepsilon kT}, \quad c = \kappa a. \tag{2.6}$$

As $Q < 0$ for the polymers comprising the glycocalyx, we have $\sigma < 0$. The dimensional potential $\Phi < 0$ everywhere, but in the dimensionless variables $\phi > 0$, $\rho = c^2\phi > 0$ and the local electric field is $+\nabla\phi$. Then the non-dimensional forms of (2.3) and (2.5) are

$$\nabla^2\phi = \rho = c^2\phi \quad \text{with} \quad \frac{\partial \phi}{\partial r} = \sigma \quad \text{on} \quad r = 1. \tag{2.7}$$

Far from the cylinder as $r \to \infty$, the potential $\phi \to 0$. The parameter c^{-1} is a non-dimensional Debye length, being the scale of exponential decay of the electrical double layer for an isolated molecule. The charged cylinder attracts oppositely signed ions from the solution which form an electrically neutralizing shield around the polyelectrolyte molecule.

It is worth observing that z-dependent charge distributions can be analysed similarly. For example, consider a charge density which varies periodically along the cylinder of the form

$$\sigma = \sigma_0 + \sigma_1 \cos kz.$$

This might be regarded as a more realistic model of a charged molecule, which contains a series of point charges along its length. Writing $\phi = \sigma_0\phi_0(r,\theta) + \sigma_1\phi_1(r,\theta)\cos kz$, then ϕ_1 satisfies

$$\nabla^2\phi_1 = \beta^2\phi_1, \quad \text{where} \quad \beta^2 = c^2 + k^2, \quad \text{with} \quad \frac{\partial \phi_1}{\partial r} = 1 \quad \text{on} \quad r = 1. \tag{2.8}$$

Thus ϕ_1 satisfies an identical problem to ϕ_0, but with a smaller value of the Debye length, as $\beta^{-1} < c^{-1}$. The exponential decay rate of ϕ_1 is therefore greater than that of ϕ_0, so that at fairly short distances from the cylinder the potential ϕ is dominated by the z-independent component. Any experimentally measurable quantities, such as osmotic pressure, will depend on the potential at some distance from the molecule. They are therefore determined by ϕ_0, and will not be affected by microscopic variation along the molecule. This argument can be generalized to any periodic charge distribution and therefore helps to justify the use of a uniformly-charged cylinder as a model for a molecule consisting of point charges.

https://doi.org/10.1017/S0022112098004030 Published online by Cambridge University Press

We now consider the solution of (2.7) in a semi-infinite square array of charged cylinders, as in figure 2. The array is unbounded as $y \to \pm\infty$, or as $x \to -\infty$, but there is a topmost layer of cylinders with centres on $x = -b$. The potential ϕ is $2b$-periodic in y, and satisfies

$$\nabla^2\phi = c^2\phi \quad \text{in} \quad |y| < b \quad \text{and} \quad r_i > 1 \quad \forall i \geqslant 0, \tag{2.9}$$

where r_i is the radial coordinate centred on the ith cylinder,

$$r_i^2 = y^2 + (x + b + 2ib)^2. \tag{2.10}$$

Far above the array of cylinders, where the immersing electrolyte solution is electrically neutral, we have $\phi \to 0$. Deep within the array, the upper boundary has little effect and ϕ tends to the solution for a fully periodic array. If we represent this as ϕ_∞, then the boundary conditions are

$$\frac{\partial\phi}{\partial r_i} = \sigma \quad \text{on} \quad r_i = 1, \quad \frac{\partial\phi}{\partial y} = 0 \quad \text{on} \quad |y| = b, \tag{2.11}$$

and

$$\phi \to 0 \quad \text{as} \quad x \to \infty, \quad \phi \to \phi_\infty \quad \text{as} \quad x \to -\infty. \tag{2.12}$$

2.1. *The numerical method*

The above problem, and corresponding ones for the Stokes equations in §§ 3 and 4, are solved using an iterative scheme similar to that of Larson & Higdon (1986, 1987). The method calculates the solution within the full domain by solving iteratively problems in square domains.

The array of cylinders can be truncated to a finite number in the x-direction, so long as sufficient cylinders remain for the solution to have tended to ϕ_∞ before the bottom-most cylinder is reached (i.e. a distance several Debye lengths from the top surface.) The domain $x < 0$, $|y| < b$ is decomposed into square domains, or cells, surrounding the cylinders, as shown on figure 2. The half-space $x > 0$ is left undivided. The last boundary condition in (2.12) for $x \to -\infty$ is equivalent to setting $\partial\phi/\partial x = 0$ on the boundary of the bottom-most square cell, owing to the symmetry of the problem for the fully-periodic array.

Within each square cell, ϕ is expressed as a function of the local polar coordinates, r_i and θ_i, where $r_i = 0$ is at the centre of the cylinder. The solution is written as a Fourier series in θ_i with coefficients which are functions of r_i. Owing to the symmetry of the solution around $y = 0$, only terms in $\cos n\theta_i$ are required. Within the upper half-space the solution is written as a Fourier series in y whose coefficients are functions of x. Again, owing to the symmetry, only terms in $\cos n\pi y/b$ are necessary. For coefficients γ_n to be found, the solution satisfying $\phi \to 0$ as $x \to \infty$, is

$$\phi = \sum_{n=0}^{\infty} \gamma_n \exp\left(-\left(c^2 + \frac{n^2\pi^2}{b^2}\right)^{1/2} x\right) \cos\frac{n\pi y}{b}. \tag{2.13}$$

After applying the boundary condition at $r_i = 1$ given in (2.12), the solution for ϕ in each square domain can be expressed as

$$\phi = \phi_i(r_i, \theta_i) \equiv \frac{\sigma}{c}\frac{K_0(cr_i)}{K_0'(c)} + \sum_{n=0}^{\infty} \alpha_{in}\left(\frac{I_n(cr_i)}{I_n'(c)} - \frac{K_n(cr_i)}{K_n'(c)}\right)\cos n\theta_i. \tag{2.14}$$

In (2.14) the subscript i denotes the square domain in which ϕ is calculated. The

https://doi.org/10.1017/S0022112098004030 Published online by Cambridge University Press

constants α_{in} are to be determined while I_n and K_n denote modified Bessel functions. The coefficients α_{in} will have different values in each square domain. For squares deep within the array ($i \to \infty$) only the terms in $\cos 4m\theta$ will have non-zero coefficients, owing to the greater symmetry.

Within each domain, the series for ϕ_i is truncated to N terms. For given boundary conditions on the edge of the square cell, applying (2.14) at M sampled points on the boundary, where $M > N$, results in an over-determined system of linear algebraic equations for the coefficients. A numerical solution was found using the LAPACK linear least-squares solver '*dgels*,' which performs a QR factorization followed by iterative refinement. Variation of the numbers M and N of boundary points sampled and of terms in the series verified the accuracy of the calculated solution.

However, in this case, the only known conditions on the solution on the boundaries A and B of each square domain (see figure 2) are that ϕ and its normal derivative ϕ_x must be continuous there. In addition, the periodicity condition $\phi_y = 0$ must be imposed explicitly on the boundaries C. This problem could be solved simultaneously for all the square cells, but the iterative procedure described below is computationally more efficient.

Each iteration starts at cell 0 (see figure 2). As a first approximation the boundary conditions on cell 0 are taken to be those imposed as $x \to \infty$ and $x \to -\infty$, that is $\phi = 0$ on the top boundary A and $\phi_x = 0$ on the bottom boundary B, together with $\phi_y = 0$ on the side boundaries, C and D. The solution for ϕ that best matches these boundary conditions can be found by truncating the infinite series expansion (2.14), applying the boundary conditions at a finite number of points around the boundary, and finding the coefficients using a least-squares method. This solution is then used to give approximations for the boundary conditions on the top of cell 1, and the bottom of the upper half-space. The solution process then passes down into the layer of cylinders, with the solution for each square cell providing the boundary conditions for the next cell. Therefore for the cells in $x < 0$, the applied boundary conditions on the zeroth iteration are

$$\phi_i^0|_A = \phi_{i-1}^0|_B, \quad \left.\frac{\partial \phi_i^0}{\partial x}\right|_B = 0, \tag{2.15}$$

where ϕ_i^j is the value of ϕ in the ith domain, on the jth iteration, and A and B are defined in figure 2.

For the upper pure-fluid half-space, the coefficients of the Fourier expansion (2.13), truncated to N terms, are found by matching values for ϕ_x at $M > N$ points at $x = 0$, and solving the resulting least-squares problem.

For successive iterations, the process is repeated, using the boundary conditions calculated from the previous iteration on boundary B of each cell. For example, for cell 0 this gives the following conditions:

$$\phi_0^{j+1}|_A = \phi_u^j|_{x=0}, \quad \left.\frac{\partial \phi_0^{j+1}}{\partial x}\right|_B = \left.\frac{\partial \phi_1^j}{\partial x}\right|_A, \tag{2.16}$$

where ϕ_u^j is the solution for ϕ in the upper half-space, $x > 0$, on the jth iteration. In the other square cells the following conditions are applied:

$$\phi_i^{j+1}|_A = \phi_{i-1}^{j+1}|_B, \quad \left.\frac{\partial \phi_i^{j+1}}{\partial x}\right|_B = \left.\frac{\partial \phi_{i+1}^j}{\partial x}\right|_A. \tag{2.17}$$

At the bottom of the lowermost square domain and the top of the upper space the

https://doi.org/10.1017/S0022112098004030 Published online by Cambridge University Press

conditions used are

$$\left.\frac{\partial \phi_i^{j+1}}{\partial x}\right|_B = \left.\frac{\partial \phi_\infty}{\partial x}\right|_A \equiv 0 \quad \text{and} \quad \left.\frac{\partial \phi_u^{j+1}}{\partial x}\right|_{x=0} = \left.\frac{\partial \phi_0^{j+1}}{\partial x}\right|_A . \tag{2.18}$$

Throughout the iterative procedure, each cell uses the values of ϕ from the current iteration on boundary A, and ϕ_x from the previous iteration on boundary B, as shown in figure 2.

Owing to the symmetry of the solution in y, only half of the solution domain, $b > y > 0$, needs to be considered throughout this process. For each iteration, the boundary points sampled for the square cells are distributed with one quarter of the points on the upper boundary A, one quarter on the lower boundary B, and the remaining half on the periodic boundary C. The sampled points are equally spaced on each boundary, with the corners omitted, and the point nearest to the corner being at a distance of 0.001. This distribution of points was found by trial and error to be the most successful over a wide range of solid concentrations. Including the corner point raises the problem as to what boundary condition to apply there. Imposing two boundary conditions at the corners gave them too great a weighting in the least-squares problem, causing convergence problems in some parameter ranges. This difficulty was resolved by placing sampled boundary points close to, but not actually at, the corners. For the half-space, $x > 0$, the boundary points are all located along the boundary $x = 0$, for $b > y > 0$. Again the corner point is omitted.

In practice, convergence is improved by using a relaxation parameter, v, and under-relaxing. Thus instead of using the boundary conditions (2.16) to solve for ϕ in cell 0, the conditions

$$\phi_0^{j+1}|_A = \frac{(\phi_u^j + v\phi_u^{j-1})|_{x=0}}{1+v}, \quad \left.\frac{\partial \phi_0^{j+1}}{\partial x}\right|_B = \frac{1}{1+v}\left(\frac{\partial \phi_1^j}{\partial x} + v\frac{\partial \phi_1^{j-1}}{\partial x}\right)\Bigg|_A , \tag{2.19}$$

are used. Similar conditions are also used for the other cells. About 5 iterations were necessary for convergence, which was most rapid over a wide range of parameter values for $v = 0.25$. The final results shown here used $N = 20$, and $M = 40$ and have a relative accuracy of 10^{-6}. The relative accuracy was determined by varying N, M and v, and comparing the results obtained.

The same method can be used when the surface charge varies with depth in the glycocalyx layer. This means that, while the array remains $2b$-periodic in the y-direction, successive cylinders deeper within the array can have different surface charge densities, $\sigma = \sigma_i$. The numerical method then proceeds exactly as described above. Similarly, the spacing between adjacent cylinders can be varied, allowing the polymer density to vary with height above the cell. In this case the domains are rectangular rather than square. The points at which the boundary conditions are imposed are chosen to be equally spaced over the domain boundary, omitting the corner points as before.

2.2. *Numerical results*

Results are presented for parameter ranges which include those found physiologically in the glycocalyx and those which are in common experimental use. Ion concentrations are expressed in molarity, so that for example a 1 M solution of salt contains Avogadro's number of sodium ions per litre. Polymer concentrations are expressed in volume fractions, $\pi/(4b^2)$. Mammalian cells are exposed to a 0.15 M ionic solution *in vivo*, and the polymer volume fraction is in the range 1–10%. The model requires the input of three parameters, namely the surface charge density of the cylinders,

https://doi.org/10.1017/S0022112098004030 Published online by Cambridge University Press

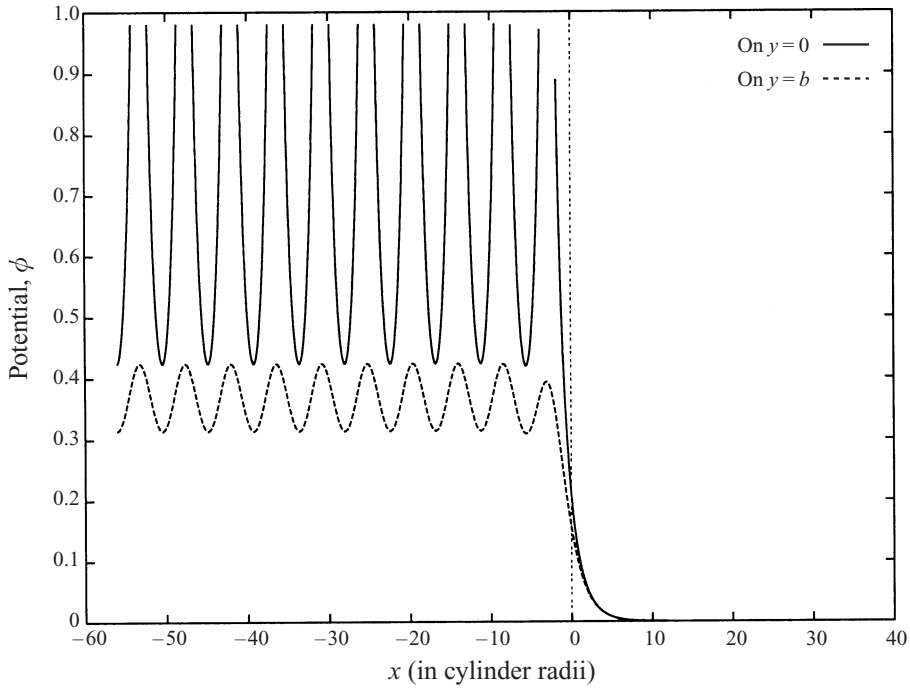


FIGURE 3. The potential ϕ for a semi-infinite square array of cylinders calculated at the centreline ($y = 0$) and between the cylinders ($y = b$). The top of the topmost cylinder is at $x = 1 - b$, as in figure 2. The polymer concentration is 10% ($b = 2.802$), and the electrolyte molarity is 0.15 M.

the radius of the cylinders, and the spacing between the cylinders or equivalently the solid volume fraction of the molecules.

The surface charge density of the cylinders depends on the molecules that are present in the glycocalyx. The biochemical data are incomplete and so we assume charges of $-e$ separated by 1.6 nm, a value measured for heparan sulphate, which is typical of the cell-surface polyelectrolytes at physiological pH (Matthews 1975).

The cylinder radius is a more difficult parameter to estimate, since it does not correspond to any real physical quantity. Throughout this paper we shall use the value $a = 0.5$ nm which is a typical size of polyelectrolyte molecules, and has been widely used throughout the literature (e.g. Buschmann & Grodzinsky 1995). In comparison, the radius of a hydrated sodium ion Na^+, surrounded by closely associated water molecules, is 0.52 nm (Kwak *et al.* 1976), while that of DNA is 0.97 nm (Gross & Strauss 1966).

Except when comparing with data from experiments performed at other temperatures, we shall use the human body temperature 310 K. Other relevant physical constants are the electron charge, $e = 1.60 \times 10^{-19}$ C, Boltzmann's constant $k = 1.38 \times 10^{-23}$ J K^{-1}, the permittivity of water, $\varepsilon = 6.91 \times 10^{-10}$ C^2 J^{-1} m^{-1} and Avogadro's number 6.02×10^{23}. Thus for a 0.15 M saline solution the Debye length $\kappa^{-1} = 0.8$ nm, while for a 10% polymer concentration, the shortest distance between cylinders is 1.8 nm.

Figure 3 shows a typical solution for the non-dimensional potential, ϕ, as calculated from (2.13) and (2.14). The curves are plotted at $y = 0$ and $y = b$, as drawn in figure 2. The discontinuities in the former correspond to the positions of the cylinders. The

https://doi.org/10.1017/S0022112098004030 Published online by Cambridge University Press

results show that the potential inside the layer tends exponentially on the scale of the Debye length towards ϕ_∞, the solution for a doubly-infinite array. This justifies the neglect of the position of the cell membrane in the model. Likewise, the potential above the cylinders decays essentially as e^{-cx}.

The potential varies notably over the surface of the uppermost cylinder owing to the asymmetry, but much less over the surfaces of the other cylinders. This variation gives rise to a resultant electrostatic force, F_i on the ith cylinder. By symmetry, this will have only an x-component, and can be thought of as the interaction of surface charge and tangential field or, in our formulation, as the net force on the charge distributed over the cylinder body. Using the Maxwell stress tensor on $r_i = 1$, this force is given by

$$F_i = -\int_0^{2\pi} \left(\sigma \frac{\partial \phi}{\partial \theta} \sin\theta + \frac{1}{2} \left(\frac{\partial \phi}{\partial \theta} \right)^2 \cos\theta \right)_{r_i=1} \mathrm{d}\theta \simeq \pi \sigma \beta_{i1}, \tag{2.20}$$

from (2.11) and (2.14), where

$$\beta_{in} = \alpha_{in} \left(\frac{I_n(c)}{I_n'(c)} - \frac{K_n(c)}{K_n'(c)} \right). \tag{2.21}$$

In (2.20) we have used the fact that except for high polymer concentrations, the radial field is dominant on the cylinder surface, $\sigma \gg \partial\phi/\partial\theta$. It is not necessary to make this approximation, but it illustrates the near equivalence of the models with distributed or surface charge. Note that $\beta_{i1} \to 0$ as $i \to \infty$. The outermost cylinders thus experience an electrostatic force repelling them from the other cylinders. In the high shielding limit, $bc \to \infty$, the force on a cylinder in the top layer is mainly due to the cylinder immediately below it. Considering two cylinders in isolation it can be shown that

$$F_0 \simeq \frac{\sigma^2 \pi^{3/2}}{c^2 K_0'(c) K_1'(c)} \frac{\mathrm{e}^{-2bc}}{(bc)^{1/2}}. \tag{2.22}$$

In addition to the electrostatic force given by (2.20), a pressure gradient must act in the system in order to maintain the equilibrium distribution of the mobile ions. This force must satisfy

$$\nabla p = \rho(\phi) \nabla \phi = c^2 \phi \nabla \phi \tag{2.23}$$

or integrating, assuming zero pressure at infinity,

$$p = \tfrac{1}{2} c^2 \phi^2. \tag{2.24}$$

It is natural to identify (2.24) as the osmotic pressure of the system. In simple geometries, such as two parallel charged plates, this expression for p can be shown to be equal to the thermodynamic osmotic pressure, but more generally the osmotic pressure is altered by additional electrical stresses due to curvature, as described in Russel, Saville & Schowalter (1989). It should in principle be possible to calculate the osmotic pressure of the glycocalyx from thermodynamic first principles using the methods described by Marcus (1955) which would be of value as it has not yet proved possible to measure it experimentally.

The additional force, G_i, on the ith cylinder due to the pressure is in the x-direction and given by

$$G_i = -\int_0^{2\pi} p \cos\theta \, \mathrm{d}\theta \simeq -\pi c^2 \beta_{i1} \left(\frac{\sigma K_0(c)}{c K_0'(c)} + \beta_{i0} \right) \tag{2.25}$$

https://doi.org/10.1017/S0022112098004030 Published online by Cambridge University Press

from (2.24), (2.20) and (2.14), neglecting other terms due to the observed rapid decay of the Fourier coefficients, $\alpha_{i2} \ll \alpha_{i0}$ etc. The total force on the ith cylinder is $F_i + G_i$. For small values of c (large Debye lengths, low molarity of electrolyte), $G_i \sim c^2 F_i$ and electrostatic repulsion of the cylinders is the dominant force. At large c, $1 \gg G_i \sim cF_i$ and the osmotic pressure is more significant, though small.

Figure 4 shows the variation of the force on the uppermost cylinders with the molarity of the surrounding salt solution and with the solid volume fraction within the glycocalyx. The force decreases dramatically as the concentration of mobile ions is decreased, and as the polymer concentration is increased. It becomes negligible when the Debye length is much less than the cylinder separation distance and the cylinders do not interact electrically. Also shown in figure 4 is the two-cylinder approximation (2.22). The repulsion between the polyelectrolyte chains must be balanced by appropriate molecular tethering to the cell membrane, which is not included explicitly in the model. These forces prevent the glycocalyx of a cell becoming too dense, as the repulsion will lead to disruption or thickening of the layer.

3. Axial flow

Because of the linearity, a general flow through the glycocalyx can be regarded as the superposition of an axial flow parallel to the cylinders and a transverse flow perpendicular to them. The former is easier to calculate and may even be more important, as it is plausible that there will be a tendency for the polyelectrolyte molecules to align themselves with the prevailing flow. Transverse flow will be considered in § 4, while in this section the flow is restricted to being in the axial direction only. Such a one-dimensional flow field could be driven by an axial shear as $x \to \infty$ or by an imposed axial electric field.

Although the blood flow is driven by a macroscopic pressure gradient, on the scale of the glycocalyx of endothelial cells lining the vessel, this can be represented totally by a shear flow at infinity. Flows driven by an imposed electric field occur in electrophoresis measurements as described in § 1. In either sort of flow, the electrical forces caused by local variation in the electric potential have no effect on the velocity, and are balanced by a local pressure gradient. Therefore, in the absence of an externally applied electric field, the fluid velocity will be unaffected by the electrical forces present in the system, and the velocity profile will be identical to that for axial flow through an array of uncharged cylinders. Such a flow will, however, give rise to a streaming current or potential, with physiological consequences as discussed in § 1.

The problem of shear-driven axial flow through a semi-infinite array of uncharged cylinders has been previously solved by Larson & Higdon (1986), providing a useful check on our computations. The main difference between their method and the one described below is that they used a boundary integral rather than spectral formulation within each subdomain. Also, they divided the whole space into square sub-domains, whereas here the upper half-space is undivided, reducing slightly the computational cost.

The flow is assumed to be governed by the Stokes equations in the presence of an electric field,

$$\nabla \cdot \boldsymbol{u} = 0, \quad \nabla p = \mu \nabla^2 \boldsymbol{u} + \rho(\nabla \phi + \boldsymbol{E}), \tag{3.1}$$

where $\boldsymbol{u}$ is the velocity, μ the constant viscosity, ϕ the potential of the ions with density ρ and $\boldsymbol{E}$ any externally imposed field. For shear-driven axial flow with no

https://doi.org/10.1017/S0022112098004030 Published online by Cambridge University Press

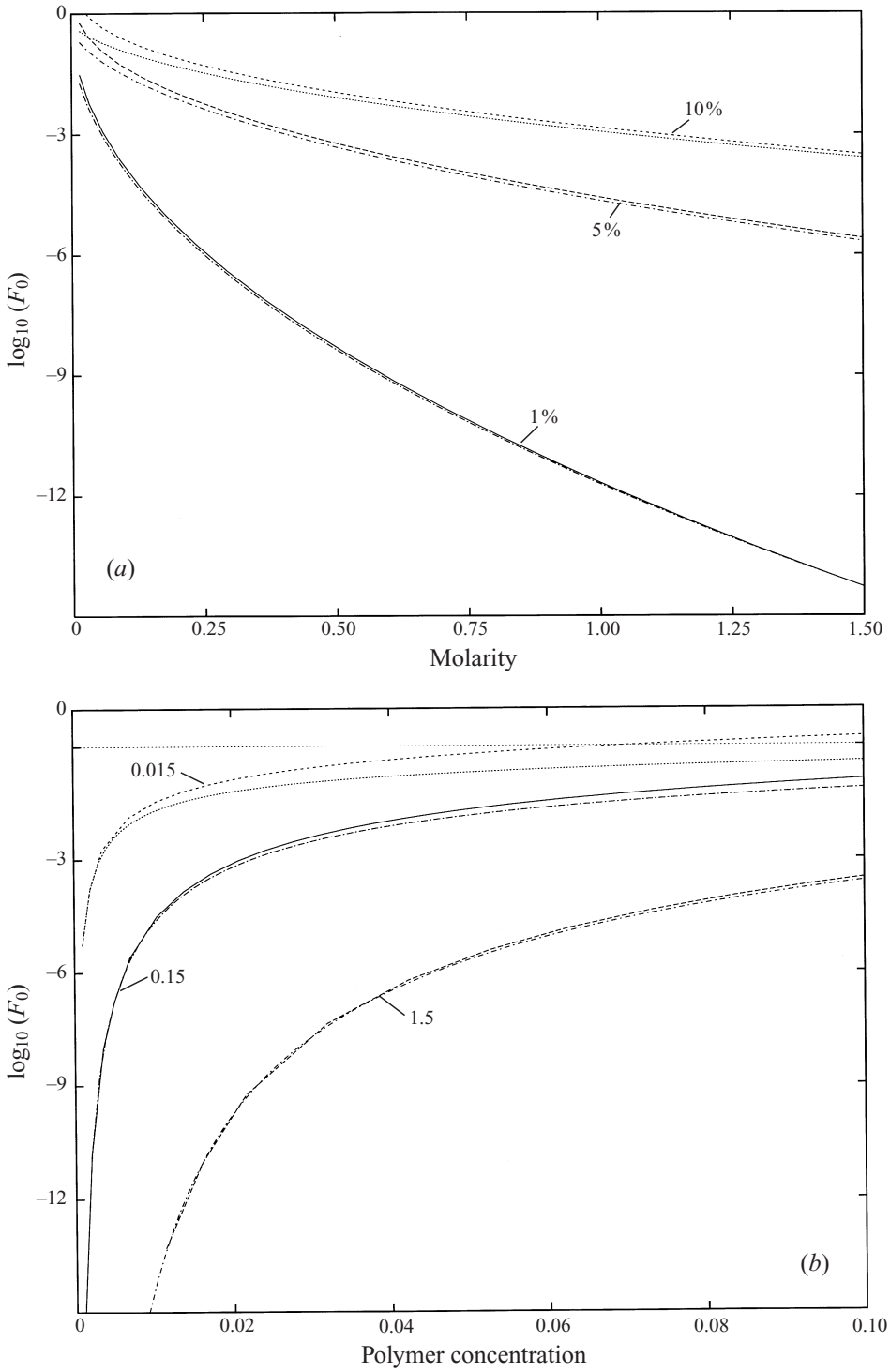


FIGURE 4. The variation of the non-dimensional force on the uppermost cylinders per unit length with (*a*) molarity, for polymer volume fractions 10%, 5% and 1%; (*b*) polymer concentration, for 0.015 M, 0.15 M and 1.5 M saline. The extreme sensitivity to the Debye length is apparent. In each case the high shielding formula (2.22) is also shown, and is indistinguishable at small Debye lengths.

https://doi.org/10.1017/S0022112098004030 Published online by Cambridge University Press

external field, $\boldsymbol{u} = (0, 0, u(x, y))$ and (3.1) reduces to

$$\nabla^2 u = 0. \tag{3.2}$$

The boundary conditions are

$$u = 0 \quad \text{on} \quad r_i = 1, \quad \frac{\partial u}{\partial x} \to \lambda \quad \text{as} \quad x \to \infty \quad \text{and} \quad u \to 0 \quad \text{as} \quad x \to -\infty, \tag{3.3}$$

where the shear rate λ is determined by the macroscopic conditions.

The solution is found using a similar decomposition method to that described in § 2 for the solution of the linearized Poisson–Boltzmann equation (2.9). Within each square sub-domain, applying the no-slip boundary condition on the cylinder surface at $r_i = 1$, u is given by

$$u(r_i, \theta_i) = \zeta_{i0} \ln r_i + \sum_{n=1}^{\infty} \zeta_{in}(r_i^n - r_i^{-n}) \cos n\theta_i. \tag{3.4}$$

In the half-space $x > 0$, the corresponding series representation with the required large-x behaviour is given by

$$u(x, y) = \eta_0 + \lambda x + \sum_{n=1}^{\infty} \eta_n \exp\left(-\frac{n\pi x}{b}\right) \cos\left(\frac{n\pi y}{b}\right). \tag{3.5}$$

As u_x is known as $x \to \infty$ and u is known as $x \to -\infty$, within each square the value of u_x from the current iteration is passed down from on top (side A in figure 2), while the previous value of u is passed up from below (side B.) The coefficients ζ_{in} and η_n are found for each domain by least-squares methods as in § 2. As the decay in (3.4) is algebraic rather than exponential, more coefficients are needed for comparable accuracy. Again, under-relaxation is needed for convergence, with $v = 0.15$ giving the best results for $N = 30$.

The results show that the velocity profile decays exponentially with depth into the array. The velocity quickly becomes self-similar for successive square cells within the array of cylinders. In fact, for all concentrations considered here, only the velocity around the top cylinder differs noticeably from the self-similar form.

Some distance above the cylinders, the velocity approaches exponentially the shear flow above a virtual plate at $x = x^*$,

$$u \to \lambda(x - x^*) \quad \text{as} \quad x \to \infty, \quad \text{where} \quad x^* = -\eta_0/\lambda. \tag{3.6}$$

Thus one effect of the glycocalyx is to move the effective cell boundary to a site about one cylinder separation distance below the top of the layer, but some distance above the actual cell membrane.

A typical solution for the axial velocity is shown in figure 5, for a solid volume fraction of 10%. The velocity in each panel of the graph is scaled to show the development of self-similar profiles for successive domains. The velocity on the symmetry line $y = b$ therefore appears discontinuous. The values of these scaling factors show that the velocity drops off more rapidly for higher polymer concentrations. The ratios between successive scaling factors for different volume fractions compare well with those calculated by Larson & Higdon (1986), as shown in figure 6. The closeness of the decay factor to unity indicates that for some purposes a Brinkman equation model might be suitable (e.g. Tsay & Weinbaum 1991). However, such an approach obscures the structure close to the molecules on which the electric streaming currents depend critically. This is even more so for the transverse flows considered in § 4.

https://doi.org/10.1017/S0022112098004030 Published online by Cambridge University Press

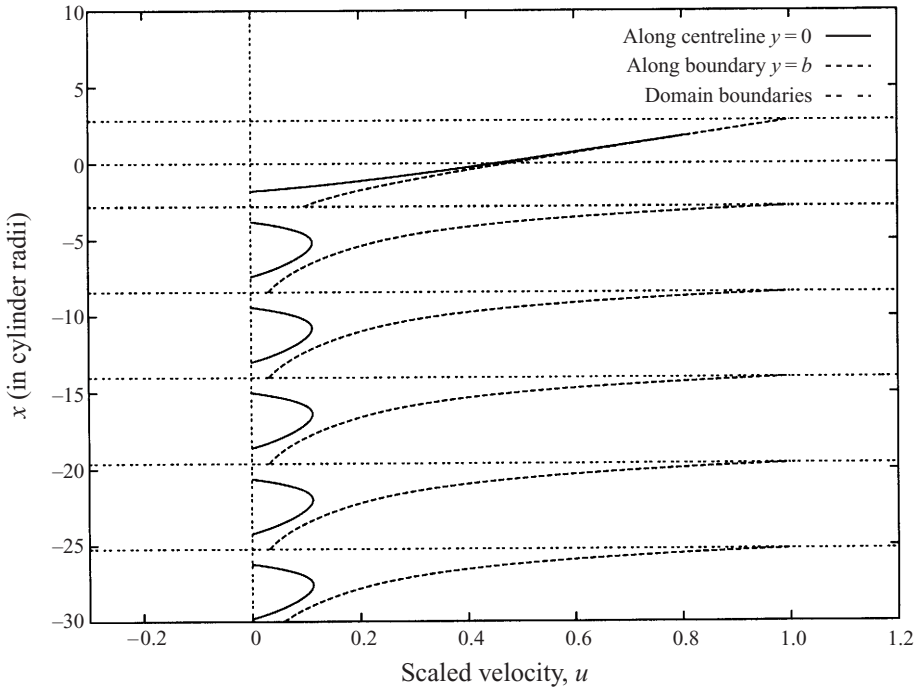


FIGURE 5. Scaled axial velocity along domain boundary $y = b$ and centreline $y = 0$ for 10% polymer concentration. The velocity is scaled for the descending square domains by the factors 0.191, 1.96, 60.2, 1860, 5.73×10^4 and 1.77×10^6, so that its self-similar structure is apparent.

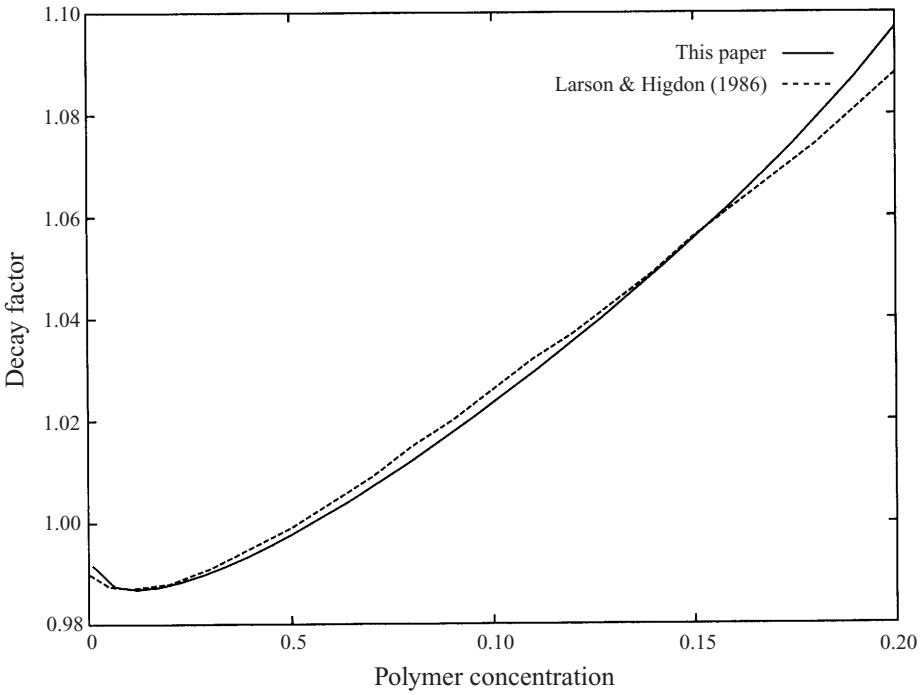


FIGURE 6. The variation with polymer concentration of the decay factor between successive square domains compared with the results of Larson & Higdon (1986).

https://doi.org/10.1017/S0022112098004030 Published online by Cambridge University Press

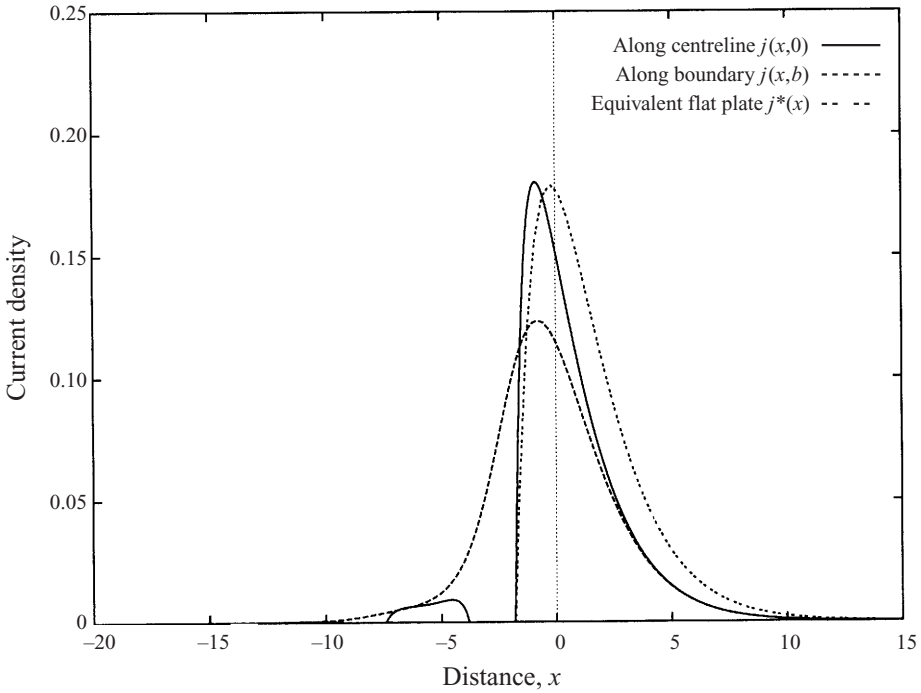


FIGURE 7. The local axial current density $j(x,0)$ and $j(x,b)$ for a semi-infinite array of cylinders and for an equivalent charged flat plate $j^*(x)$ (see text: $x^* = -1.802$, $\sigma^* = 0.487$). The calculation is performed for unit shear at infinity, a 10% polymer concentration and a 0.15 M monovalent electrolyte, so that $c = 0.6263$.

3.1. *The streaming current and streaming potential*

When mobile ions are present in the moving fluid, the axial flow field will also generate an electric current as the ions move with the fluid. Such a current is known as a 'streaming current'. Very often, the current paths close by means of bulk conduction within the main body of the fluid. For this to occur, a potential difference must be set up along the cylinders, called a streaming potential.

The non-dimensional streaming current density, $j(x, y)$, is in the z-direction and is given by

$$j = \rho u = c^2 \phi u, \tag{3.7}$$

where u is as found above for axial flow, and ϕ is given in (2.13) and (2.14). This gives a total axial current per unit glycocalyx length of

$$J_{ax} = \frac{c^2}{b} \int_0^b \int_{-\infty}^{\infty} \phi u \, \mathrm{d}x \, \mathrm{d}y \tag{3.8}$$

(defining $u \equiv 0$ inside the cylinders).

The local streaming current given by (3.7) is zero far from the glycocalyx (where $\phi \to 0$) and also deep within the glycocalyx (where $u \to 0$). A typical graph of the local current density is shown in figure 7 for a volume fraction of 10% and an electrolyte concentration of 0.15 M. This shows that the only significant contribution to the total current comes from the fluid surrounding the top one or two cylinders in the array. This is important in practice, because it means that experimental data on streaming potentials can only give information about the charge density of the outermost part

https://doi.org/10.1017/S0022112098004030 Published online by Cambridge University Press

of the glycocalyx. It also confirms the implicit assumption in the model that the lower boundary of the glycocalyx (the cell surface) is unimportant in determining quantities which can be measured experimentally, and so can be neglected in the model without significant effect.

The streaming current can be compared with that which would occur over a charged plate at $x = x^*$. The value of x^* could be chosen to be the hydrodynamical value as given by (3.6). In fact, below we shall use the value $x^* = 1-b$, corresponding to a flat plate resting on top of the uppermost cylinders (recall that the centres of the uppermost cylinders are at $x = -b$.) If the plate carries a charge density σ^*, then the corresponding potential $\phi^*(x)$ and current density $j^*(x)$ are given in $x > x^*$ by

$$\phi^* = -\frac{\sigma^*}{c}\mathrm{e}^{-c(x-x^*)} \quad \text{and} \quad j^* = -c\lambda\sigma^*(x-x^*)\mathrm{e}^{-c(x-x^*)}, \tag{3.9}$$

using (3.6). The appropriate charge density σ^* could be chosen to give rise to the same total streaming current, or the same molecular charge per unit length as one row of cylinders. Figure 7 includes a graph of $j^*(x)$ with σ^* chosen so that $j^*(x)$ has the same maximum value as $j(x)$. It can be seen that the flat-plate current attains this maximum value at a larger value of x than does the cylinder current, as the velocity close to a flat plate is lower than the velocity at the same distance above an array of cylinders.

Figure 8(a) shows the effect on the total streaming current of varying the polymer concentration and the molarity of the surrounding electrolyte. As described above, the majority of this current is generated by the fluid surrounding the topmost layer of cylinders only, and therefore will vary linearly with the charge density of the uppermost cylinders. At low concentrations of electrolyte, or at high volume fractions of polymer, when the Debye length is comparable to the spacing between the cylinders, the potentials within the glycocalyx are greatest, and hence so is the current generated. At high electrolyte concentrations, when the Debye length is much less than the spacing between the cylinders, the potential will only be non-zero close to each cylinder. The generated current then depends only on the region close to each cylinder, and hence is independent of polymer concentration.

3.2. *Electrophoretic mobility*

The electrophoretic mobility of a biological cell is the steady velocity it attains when placed in a uniform electric field. A negatively-charged cell such as a red blood cell or endothelial cell will have a negative electrophoretic mobility.

The cell and all the attached cylinders are assumed to move at a constant velocity under the influence of an externally applied electric field, $(0, 0, -E)$. The Stokes equation (3.1) for the axial fluid velocity, $u(x, y)$, is

$$\mu\nabla^2 u = \rho E = Ec^2\phi, \tag{3.10}$$

where ϕ is the electric potential due to local variations in the ion distributions, calculated in § 2 from the linearized Poisson–Boltzmann equation. In a frame with the cylinders at rest, the boundary conditions are

$$u = 0 \quad \text{on} \quad r_i = 1, \quad u \to 0 \quad \text{as} \quad x \to -\infty \quad \text{and} \quad u_x \to 0 \quad \text{as} \quad x \to \infty. \tag{3.11}$$

As $x \to \infty$, u approaches a value u_0, to be calculated, which is the electrophoretic velocity.

We note that equation (3.10) is similar to (2.9) and hence that a particular solution is $u = E\phi/\mu$. The solution satisfying the requisite boundary conditions can therefore

https://doi.org/10.1017/S0022112098004030 Published online by Cambridge University Press

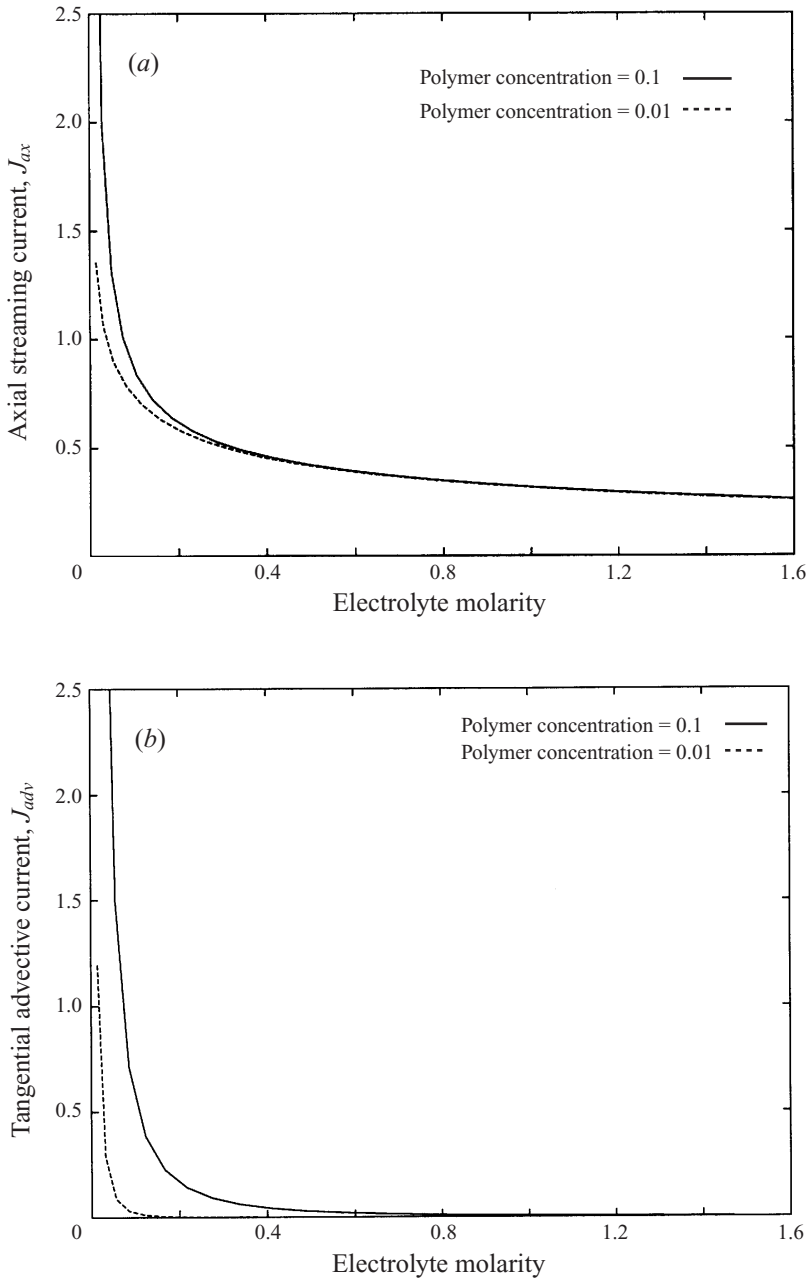


FIGURE 8. The variation with molarity of (*a*) the total axial streaming current, J_{ax}, (*b*) the advective part of the transverse streaming current, J_{adv}, for unit shear ($\lambda = 1$) and polymer concentrations of 1% and 10%.

be found by adding on a suitable harmonic function, in the same way as in the absence of electrical effects. Since ϕ is uniform in the z-direction, the applied electric field does not perturb the distribution of mobile ions or the electric potential from the equilibrium values calculated using the Poisson–Boltzmann equation (2.9).

After applying the no-slip boundary condition on the cylinders at $r = 1$, noting

https://doi.org/10.1017/S0022112098004030 Published online by Cambridge University Press

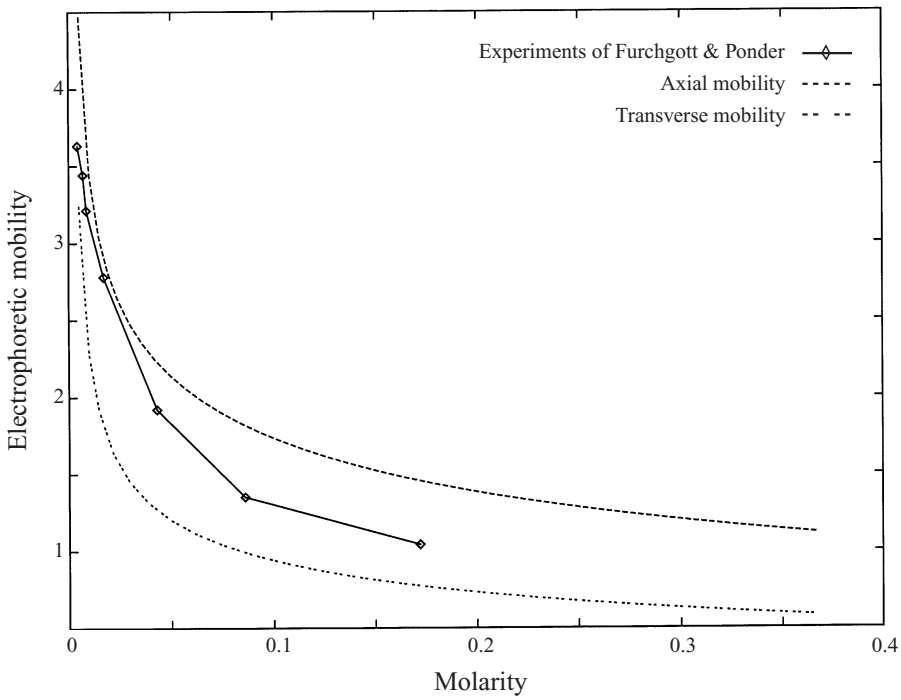


FIGURE 9. The variation of electrophoretic mobility with molarity, for a 1% polymer concentration. Experimental data from Furchgott & Ponder (1941) lie between our predictions for axial and transverse flows.

that $\phi \neq 0$ there, the expansions for u in the square sub-domains take the form

$$u(r_i, \theta_i) = \zeta_{i0} \ln r_i + \sum_{n=1}^{\infty} \zeta_{in}(r_i^n - r_i^{-n}) \cos n\theta_i + \frac{E}{\mu}\left(\phi_i(r_i, \theta_i) - \frac{\sigma}{c}\frac{K_n(c)}{K_n'(c)} + \sum_{n=0}^{\infty} \beta_{in} r^{-n} \cos n\theta_i\right) \tag{3.12}$$

where β_{in} are as given in (2.21) for the α_{in} as found from (2.14). The series expansion in the half-space $x > 0$, with the required large-x behaviour, is

$$u(x, y) = u_0 + \sum_{n=1}^{\infty} \eta_n \exp\left(-\frac{n\pi x}{b}\right) \cos\left(\frac{n\pi y}{b}\right) + E\phi(x, y), \tag{3.13}$$

where $\phi(x, y)$ is the solution (2.13) calculated above.

The unknown coefficients u_0, ζ_{in} and η_n, are found as previously. The iterative method proceeds as before, with the values from the previous iteration of u and u_x being passed respectively up from the bottom and down from the top. Under-relaxation is once more required for convergence. A representative solution for the electrophoretic mobility u_0/E is shown in figure 9, where it is compared with experiments and the electrophoretic mobility for a field transverse to the cylinders, as discussed in the following section.

https://doi.org/10.1017/S0022112098004030 Published online by Cambridge University Press

4. Transverse flow

In this section the flow is restricted to be in the plane perpendicular to the cylinder axes. This two-dimensional flow field, $\boldsymbol{u} = (u, v, 0)$, satisfies the Stokes equations

$$\mu\nabla^2\boldsymbol{u} = \nabla p - c^2\phi\nabla\phi, \quad \nabla\cdot\boldsymbol{u} = 0 \tag{4.1}$$

where p is the pressure and the potential ϕ satisfies the linearized Poisson–Boltzmann equation (2.7). For flow driven by a shear of strength λ above the array of cylinders, no net pressure gradient acts. The electric force is conservative, and merely gives rise to an osmotic pressure as in (2.11). Taking the curl of (4.1) and defining a streamfunction by $\boldsymbol{u} = \nabla\wedge(0, 0, \psi)$, the flow can be represented by

$$\nabla^2\psi = -\omega, \quad \nabla^2\omega = 0, \tag{4.2}$$

where the vorticity $\nabla\wedge\boldsymbol{u} = (0, 0, \omega)$. The associated boundary conditions on the cylinders are

$$\frac{\partial\psi}{\partial r_i} = \frac{\partial\psi}{\partial\theta_i} = 0 \quad \text{on} \quad r_i = 1, \tag{4.3}$$

at top and bottom

$$\frac{\partial^2\psi}{\partial x^2} \to \lambda \quad \text{as} \quad x\to\infty \quad \text{and} \quad \frac{\partial\psi}{\partial x} \to 0 \quad \text{as} \quad x\to-\infty, \tag{4.4}$$

and on the symmetry lines

$$\frac{\partial\psi}{\partial y} = \frac{\partial\omega}{\partial y} = 0 \quad \text{on} \quad |y| = b. \tag{4.5}$$

In the ith cylinder domain, the vorticity is expanded as

$$-\omega = f_{i0} + g_{i0}(\ln r_i + 1) + \sum_{n=1}^{\infty}\left(f_{in}r_i^n + g_{in}r_i^{-n}\right)\cos n\theta_i. \tag{4.6}$$

Below, we shall suppress the suffix i for clarity. It is not possible to solve for the vorticity directly, since there are no boundary conditions on ω at $r = 1$. The corresponding expansion for ψ, satisfying $\psi_r = \psi_\theta = 0$ on $r = 1$, is

$$\begin{aligned}\psi = {} & A + \tfrac{1}{4}f_0(r^2 - 2\ln r - 1) + \tfrac{1}{4}g_0 r^2\ln r \\ & + \left[\tfrac{1}{8}f_1(r^2 - 2r + r^{-1}) + \tfrac{1}{4}g_1(2r\ln r - r + r^{-1})\right]\cos\theta \\ & + \frac{1}{4}\sum_{n=2}^{\infty}\left[f_n\left(\frac{r^{n+2}}{n+1} - \frac{r^n}{n} + \frac{r^{-n}}{n(n+1)}\right) + g_n\left(\frac{r^{2-n}}{1-n} - \frac{r^n}{n(1-n)} + \frac{r^{-n}}{n}\right)\right]\cos n\theta.\end{aligned} \tag{4.7}$$

In $x > 0$ the expansions are

$$-\omega = \lambda + \sum_{n=1}^{\infty} a_n\cos\left(\frac{n\pi y}{b}\right)\exp\left(-\frac{n\pi x}{b}\right) \tag{4.8}$$

and

$$\psi = B + \tfrac{1}{2}\lambda x^2 + b_0 x + \sum_{n=1}^{\infty}\left(b_n - \tfrac{1}{2}a_n x\frac{b}{n\pi}\right)\cos\left(\frac{n\pi y}{b}\right)\exp\left(-\frac{n\pi x}{b}\right). \tag{4.9}$$

https://doi.org/10.1017/S0022112098004030 Published online by Cambridge University Press

We normalize ψ by setting $B = 0$. There is still one too many unknown coefficients and another condition must be imposed before applying the symmetry conditions on $y = b$. This is because the domain is not simply connected, and the solution as given in (4.7) does not necessarily satisfy the condition that the pressure, p, be a single-valued function of θ. This condition can be expressed as

$$\int_0^{2\pi} \frac{\partial p}{\partial \theta_i}\Big|_{r_i=1} \mathrm{d}\theta_i = 0 \quad \text{or} \quad \int_0^{2\pi} \frac{\partial \omega}{\partial r_i}\Big|_{r_i=1} \mathrm{d}\theta_i = 0 \tag{4.10}$$

from (4.1), which with (4.6) implies

$$g_{i0} = 0. \tag{4.11}$$

The Fourier series are truncated to N terms so that the coefficients can be found numerically. This is done as before, by sampling the boundary conditions at $M > N$ points around the outer boundary. The difference is that in this case two boundary conditions are imposed at each sampled point, essentially one on ψ and one on ω. A similar method was used by Sangani & Acrivos (1982) to solve for the pressure-gradient-driven transverse Stokes flow in a doubly-periodic square array of cylinders in the absence of electric charge.

As before, an iterative technique is used for the boundary conditions at the artificial boundaries dividing adjacent square domains. The values of ψ_{xx} and ψ are passed down from the current iteration and those of ψ_x and ψ_{xxx} are passed up from the previous iteration. Under-relaxation is required for convergence, with a relaxation parameter $v = 0.2$ giving the best results for $N = 30$.

This problem was also solved by Larson & Higdon (1987), using the same iterative method but with a boundary integral formulation within each square domain. The results are once more in good agreement and are not repeated here. The flow structure is more complex than in the axial case, with regions of closed streamlines.

4.1. *Streaming current and potential*

Streaming current calculations are carried out for transverse shear flow at infinity, in the absence of an externally-applied electric field. We neglect any distortion of the distribution of mobile ions due to the movement of the surrounding fluid. This in effect assumes that Brownian diffusion of ions instantaneously replaces any ions advected by the motion. As discussed by Sherwood (1980, 1981), this implies the existence of an additional current given by a function $\Omega(x, y)$ such that the local streaming current density, $\boldsymbol{j}(x, y)$, is given by

$$\boldsymbol{j} = \rho \boldsymbol{u} + \nabla\Omega = c^2\phi\boldsymbol{u} + \nabla\Omega. \tag{4.12}$$

Charge conservation requires $\nabla \cdot \boldsymbol{j} = 0$, so that outside the cylinders

$$\nabla^2\Omega = -c^2\boldsymbol{u} \cdot \nabla\phi, \tag{4.13}$$

a known function as ϕ and $\boldsymbol{u}$ are known. The symmetry, periodicity and the requirement of no current flow into the cylinders lead to the boundary conditions

$$\frac{\partial\Omega}{\partial r_i} = 0 \quad \text{on} \quad r_i = 1 \quad \text{and} \quad \Omega = 0 \quad \text{on} \quad y = \pm b. \tag{4.14}$$

Equations (4.13) and (4.14) determine the extra current uniquely. On physical grounds, one might expect this current to resist the fluid-induced distortion of the ion cloud, leading to a lower transverse streaming current than in the axial case. The advective

https://doi.org/10.1017/S0022112098004030 Published online by Cambridge University Press

electric current across $y = b$ per unit length along the cylinders, J_{adv}, is in the y-direction,

$$J_{adv} = -\int_{-\infty}^{\infty} c^2 \phi(x,b) \frac{\partial \psi}{\partial x}(x,b)\,\mathrm{d}x. \tag{4.15}$$

J_{adv} is plotted as a function of molarity in figure 8(b) for volume fractions of 1% and 10% and unit transverse shear ($\lambda = 1$). Comparison with figure 8(a) indicates the much more rapid falling off with molarity, as expected because on $y = b$ at large c, $\phi \sim \exp(-cb)$.

The total transverse streaming current per unit cylinder length, $J_{tr} = J_{adv} + J_B$, where the extra current

$$J_B = \int_{-\infty}^{\infty} \frac{\partial \Omega}{\partial y}(x,b)\,\mathrm{d}x, \tag{4.16}$$

follows from the solution of (4.13) with (4.14).

The asymptotic form of J_B may be derived in the small Debye length limit, $c \to \infty$. The source term in (2.3) is then localized to a layer of thickness c^{-1} about the cylinders. On this short length scale, the streamfunction can be approximated as

$$\psi = -\tfrac{1}{2} n^2 \omega_s(\theta) + O(c^{-1}), \quad \text{where} \quad n = r_i - 1 \tag{4.17}$$

and $\omega_s(\theta)$ is the surface vorticity given by (4.6) on $r_i = 1$. We know that the contribution from the top layer of cylinders ($i = 0$) will dominate. The potential ϕ in (2.14) is almost radially symmetric,

$$\phi \simeq -\frac{\sigma}{c} \mathrm{e}^{-cn} + O(c^{-1}), \tag{4.18}$$

so that from (4.18) and (4.17) the solution of (4.13) to leading order in c^{-1} can be written

$$\Omega = \tfrac{1}{2} c^{-2} \sigma \omega_s'(\theta) \left(c^2 n^2 + 4cn + 6\right) \mathrm{e}^{-cn} + \overline{\Omega}, \tag{4.19}$$

where $\overline{\Omega}$ is determined by

$$\nabla^2 \overline{\Omega} = 0\,, \qquad \overline{\Omega} = 0 \quad \text{on} \quad y = \pm b \quad \text{and} \quad \frac{\partial \overline{\Omega}}{\partial r_i} = \frac{\sigma}{c} \omega_s'(\theta) \quad \text{on} \quad r_i = 1. \tag{4.20}$$

Now by Green's theorem applied to $y\nabla^2 \overline{\Omega} - \overline{\Omega} \nabla^2 y$,

$$2bJ_B = \int_{y=\pm b} y \frac{\partial \overline{\Omega}}{\partial y}\,\mathrm{d}x = -\oint_{r_i=1} \left(y \frac{\partial \overline{\Omega}}{\partial r} - \overline{\Omega} \frac{\partial y}{\partial r} \right) \mathrm{d}\theta = \int_0^{2\pi} \sin\theta (\overline{\Omega} - \overline{\Omega}_r)\big|_{r_i=1}\,\mathrm{d}\theta. \tag{4.21}$$

Thus only the first harmonic of $\overline{\Omega}$ contributes to the streaming current. A cylindrical cell approximation requiring $\overline{\Omega} = 0$ on $r = b_0$ leads to the estimate for the streaming current for large c,

$$J_{tr} \simeq J_B \simeq \sum_{i=0}^{\infty} \frac{\pi\sigma}{cb} \frac{(f_{i1} + g_{i1})}{(1 + 1/b_0^2)} \simeq \frac{\pi\sigma}{cb} \frac{(f_{01} + g_{01})}{(1 + 1/b_0^2)}, \tag{4.22}$$

where f_{i1} and g_{i1} are as found from (4.6). A similar calculation for the axial streaming current of (3.7) would give

$$J_{ax} = \frac{c^2}{b} \int \phi u\,\mathrm{d}x\,\mathrm{d}y \simeq \frac{c^2}{b} \int \frac{\sigma}{c} \mathrm{e}^{-cn} \zeta_{00} n\,\mathrm{d}n\,\mathrm{d}\theta = \frac{2\pi\sigma}{cb} \zeta_{00}, \tag{4.23}$$

where ζ_{00} is as given by (3.4). We conclude that for small Debye lengths, the streaming

https://doi.org/10.1017/S0022112098004030 Published online by Cambridge University Press

current is formally of the same small order for both axial and transverse flows. However, hydrodynamical effects control the numerical coefficients and ensure that the axial current is significantly larger.

4.2. *Electrophoretic mobility*

We suppose that an external electric field $\boldsymbol{E} = (0, -E, 0)$ is applied parallel to the cell surface, in a direction perpendicular to the cylinder axes. As in § 3, we use a frame with the cell at rest, while the fluid far from the cylinders moves at a uniform velocity. The motion is now given by

$$\nabla \cdot \boldsymbol{u} = 0 \quad \text{and} \quad \mu \nabla^2 \boldsymbol{u} = \nabla p - c^2 \phi (\boldsymbol{E} + \nabla \phi). \tag{4.24}$$

As before, ϕ is assumed to equal the equilibrium potential from the linearized Poisson–Boltzmann equation, given by (2.13) and (2.14). The imposed field, E, may well be much greater than $|\nabla \phi|$, when the last term in (4.24) could be neglected. However, there is no need to do so as this term merely modifies the pressure distribution.

In terms of the vorticity, ω, and the streamfunction, ψ, (4.24) takes the form

$$\nabla^2 \psi = -\omega, \quad \nabla^2 \omega = \frac{c^2 E}{\mu} \frac{\partial \phi}{\partial x}. \tag{4.25}$$

As before, the solutions are represented as Fourier series in θ_i for the sub-domains around the cylinders, and in y for the half-space above the layer of cylinders. Comparison with (3.10) indicates that a particular solution for the vorticity is

$$\omega = \frac{E}{\mu} \frac{\partial \phi}{\partial x}, \tag{4.26}$$

as the x-derivative commutes with the Laplacian. Thus ω may be expanded as

$$\omega = f_{i0} + g_{i0}(\ln r_i + 1) + \sum_{n=1}^{\infty} \left(f_{in} r_i^n + g_{in} r_i^{-n} \right) \cos n\theta_i + \frac{E}{\mu} \left(\cos\theta \frac{\partial \phi}{\partial r} - \frac{1}{r} \sin\theta \frac{\partial \phi}{\partial \theta} \right). \tag{4.27}$$

The condition that p is a single-valued function of θ_i must again be explicitly applied. In fact, this condition reduces once more to

$$g_{i0} = 0. \tag{4.28}$$

Using (2.14), an expansion for ψ similar to (4.7) satisfying the conditions $\psi_r = \psi_\theta = 0$ on the cylinders can now be found. Likewise, ψ and ω for $x > 0$ follow from (4.26), (4.8) and (4.9). The familiar truncation and iteration procedure solves the problem. The resultant electrophoretic velocities are plotted as a function of molarity in figure 9. It is apparent that these are smaller than the corresponding results for axial flows.

4.3. *Combination of axial and transverse results*

In reality the polyelectrolyte chains are not all parallel, as assumed by our model. Furthermore, a general flow will have both axial and transverse components. Thus a suitable average of the transverse and axial results may well be more appropriate, but it is not obvious what mean to take. For an uncharged, infinite, isotropic medium, Jackson & James (1986) proposed a weighting of one-third axial and two-thirds transverse. In the glycocalyx there will be few polyelectrolyte chains perpendicular to the cell surface, so the equivalent assumption is a 50:50 split between axial and transverse flow directions. Bearing in mind the nonlinear dependence with the volume fraction, such calculations should probably be performed at half concentrations for

https://doi.org/10.1017/S0022112098004030 Published online by Cambridge University Press

each of the axial and transverse cases, rather than averaging the results at full concentration. However, there may well be a tendency for molecules to align with the prevailing flow, giving a greater number of axial molecules. This is especially the case for charged molecules, which are likely to be straighter.

Figure 9 compares our calculated results with some experimental measurements from Furchgott & Ponder (1941). It is apparent that the experimental data fall between the axial and transverse curves, and so an average could give excellent agreement.

5. Implications and limitations

The model of a continuum of ions surrounding a semi-infinite array of charged cylinders gives reasonably good agreement with experimental measurements of the glycocalyx, both as regards electrophoretic mobilities of red cells and streaming potentials in blood vessels.

An important conclusion from the model is that streaming currents and electrophoretic mobilities are determined by the structure and behaviour of only the outermost portion of the glycocalyx, and therefore give no information about conditions near the cell surface. There is thus a limit as to what experimental measurements of this kind can indicate about the biochemical structure of the glycocalyx. Our model is independent of the depth of the glycocalyx, in contrast to some one-dimensional models which require this depth as a parameter and are sensitive to its value. Indeed, once the flexible nature of the glycoproteins is taken into account, the thickness of the glycocalyx will be predicted by our model. Our predictions are compared with those of Levine *et al.* (1983) in Mestel *et al.* (1999).

Once the electrostatic potentials are known, the distributions of the different species of mobile ions present can be calculated, as described in Mestel *et al.* (1999). Just as for the potential, the ion distribution only deviates from that for a doubly-periodic array close to the surface of the array of cylinders. This means that close to the surface of a biological cell, at the base of the glycocalyx, the ion concentrations will be unaffected by the finite depth of the glycocalyx, assuming that it is deeper than two or three Debye lengths. Therefore, the fully periodic potential ϕ_∞ can be used to predict the ionic atmosphere with which the cell itself is in equilibrium, but this differs from the ion distribution at the top of the layer, which controls the electrokinetic behaviour.

It is still unclear how much charge is carried on the cell membrane itself rather than on the glycocalyx. However, in the parameter ranges of physiological and experimental interest, for arrays of three or more cylinders in depth, the addition of further cylinders has no significant effect on the calculated potential around the uppermost three cylinders. Similarly, if the cell membrane at say $x = -d$ is charged, then it is equivalent to the boundary condition

$$\frac{\partial \phi}{\partial x} = q \quad \text{on} \quad x = -d,$$

where q represents the surface charge of the cell membrane. If q is small compared to the charge density of the cylinders, then this will have little effect. Even if $q \simeq \sigma$ it will only affect the potential close to the cell membrane itself. The potential at the top of the glycocalyx will be affected by q only if the depth of the model layer is fewer than 5 cylinders.

The use of the Poisson–Boltzmann equation in the analysis merits discussion. It treats the mobile ions as a continuum, assuming in effect that the mobile ions are

https://doi.org/10.1017/S0022112098004030 Published online by Cambridge University Press

small relative to the radius of the cylindrical polyelectrolyte ion. It also neglects direct interactions between the different species of mobile ion, and between adjacent polyions. In addition, the derivation of the equation assumes that the system of mobile ions is in thermal equilibrium, even though the surrounding solute is in motion. This latter assumption is valid provided the thermal energy of ions is much larger than the work required to move them, or

$$6\pi\mu\lambda L^3 \ll kT,$$

where μ is the viscosity of the fluid, λ a typical shear rate, and L a relevant length scale. This constraint is trivially satisfied on the molecular length scale $L = 0.5$ nm for shear stresses in the circulation for which $\mu\lambda \ll 40$ N m^{-2} (Pedley 1980). Perturbations to the equilibrium charge cloud were considered by Sherwood (1980, 1981).

In general, the mobile monovalent ions are smaller than the polyions, even in hydrated form, but they are of the same order of magnitude. The validity of the Poisson–Boltzmann equation on these length scales has been investigated in various ways. Fixman (1979) examined the effects of finite ion size and direct ion–ion interactions, while other investigations have compared the Poisson–Boltzmann equation predictions with those of Monte Carlo methods (e.g. Le Bret & Zimm 1984). These investigations suggest that the Poisson–Boltzmann equation works well for small monovalent counter-ions in low enough concentrations, but under-predicts the concentrations of co-ions close to the cylinder. They also show that the Poisson–Boltzmann approximation is less good for large ions, with radius similar to that of the cylinder, or in concentrated solutions of ions, since in these cases the ion distributions are dominated by steric effects, which are neglected in the derivation of the Poisson–Boltzmann equation. Discrepancies between the predictions of Monte-Carlo methods and those of the Poisson–Boltzmann equation also arise when the ions are multivalent. Some of the discrepancies with Monte-Carlo methods can be addressed by modifying the Poisson–Boltzmann equation (e.g. Haydon 1964). Including a finite ion radius could also introduce electro-osmotic coupling between the ions and the fluid (Derjaguin & Dukhin 1974).

In this paper we have linearized the Poisson–Boltzmann equation, which is a valid approximation in most physiological contexts. Comparison with results from the full nonlinear equation, and with cylindrical cell and line-charge models, are presented elsewhere (Mestel *et al.* 1999). Cylindrical cell approximations give reasonable results for the potential but are less accurate for hydrodynamic quantities, because of the slower rate of decay from the cylinder surface.

Finally, we discuss the use of the Stokes equations in calculating the flow. The fluid consists mainly of water and mobile ions and it is assumed that this mixture can be represented by a continuum on length scales close to those of the individual ions and water molecules. This effectively assumes that the concentration of ions is low enough that there are no volume exclusion effects, and that the ions move at the same velocity as adjacent water molecules. This assumption merits further investigation by comparing the predictions of the continuum model with those of, for example, Monte Carlo methods, but this is beyond the scope of this paper.

Although blood itself is non-Newtonian at small shear rates, this is mainly because of the presence of the red cells. On scales much shorter than the diameter of these red cells it is reasonable to treat the blood plasma as Newtonian. Osmotic effects due to exclusion of blood proteins from the glycocalyx are neglected. The use of a no-slip boundary conditions on the surface of the cylinders is again an assumption worthy of closer investigation. On a molecular level it is not certain how water molecules

https://doi.org/10.1017/S0022112098004030 Published online by Cambridge University Press

will interact with a polyelectrolyte ion when moving past it. As the model presented here already approximates the complex shape of the polyelectrolyte ions by a simple cylinder, it is unlikely that the no-slip condition would introduce significant further error, provided an appropriate value for the radius a is taken.

A. Mokady was supported by a Prize Studentship in Mathematical Biology awarded by the Wellcome Trust.

REFERENCES

Buschmann, M. D. & Grodzinsky, A. J. 1995 A molecular model of proteoglycan associated electrostatic forces in cartlage mechanics. *J. Biomech. Engng* **117**, 179–192.

Davies, P. F. 1995 Flow mediated endothelial mechano-transduction. *Physiol. Rev.* **75**, 519–558.

Derjaguin, B. V. & Dukhin, S. S. 1974 Equilibrium double layer and electrokinetic phenomena. In *Surface and Colloid Science*, Vol. 7 (ed. E. Matijevic), pp. 49–272. Wiley.

Desjardins, C. & Duling, B. R. 1990 Heparinase treatment suggests a role for the endothelial cell glycocalyx in regulation of capillary hematocrit. *Am. J. Physiol.* **258** (*Heart Circ. Physiol.* **27**), H647–H654.

Drummond, J. E. & Tahir, M. I. 1984 Laminar viscous flow through regular arrays of parallel solid cylinders. *Intl J. Multiphase Flow* **10**, 515–540.

Edwards, D. A. 1995 Charge transport through a spatially periodic porous medium: electrokinetic and convective dispersion phenomena. *Phil. Trans. R. Soc. Lond.* A **353**, 205–242.

Fixman, M. 1979 The Poisson–Boltzmann equation and its application to polyelectrolytes. *J. Chem. Phys.* **70**, 4995–5005.

Furchgott, R. F. & Ponder, E. 1941 Electrophoretic studies on human red blood cells. *J. Gen. Physiol.* **24**, 447–457.

Gross, L. M. & Strauss, U. P. 1966 Interactions of polyelectrolytes with simple electrolytes. I. Theory of electrostatic potential and Donnan equilibrium for a cylindrical rod model: the effect of site binding. In *Chemical Physics of Ionic solutions* (ed. B. E. Conway & R. G. Barradas). Plenum.

Happel, J. 1957 Viscosity of suspensions of uniform spheres. *J. Appl. Phys.* **28**, 1288–1292.

Happel, J. 1958 Flow in multiparticle systems: slow motion of fluids relative to beds of spherical particles. *AIChE J.* **4**, 197–201.

Happel, J. 1959 Viscous flow relative to arrays of cylinders. *AIChE J.* **5**, 174–177.

Haydon, D. A. 1964 The electrical double layer and electrokinetic phenomena. *Recent Prog. Surf. Sci.* **1**, 94–158.

Jackson, G. W. & James, D. F. 1986 The permeability of fibrous porous media. *Can. J. Chem. Engng* **64**, 364–374.

Katchalsky, A. 1971 Polyelectrolytes. *Pure Appl. Chem.* **26**, 327–373.

Kuhn, W., Kunzle, O. & Katchalsky, A. 1948 Verhalten polyvanter fadenmolekelionen in losung. *Helvet. Chim. Acta* **31**, 1994–2037.

Kwak, J. C. T., Morrison, N. J., Spiro, E. J. & Iwasa, K. 1976 Mean activity coefficients for the simple electrolyte in aqueous mixtures of polyelectrolyte and simple electrolyte. The mixed counterion system Na^+, Ca^{2+}, Cl^-, polystyrene-sulfonate. *J. Phys. Chem.* **80**, 2753.

Larson, R. E. & Higdon, J. J. L. 1986 Microscopic flow near the surface of two-dimensional porous media. Part 1. Axial Flow. *J. Fluid Mech.* **166**, 449–472.

Larson, R. E. & Higdon, J. J. L. 1987 Microscopic flow near the surface of two-dimensional porous media. Part 2. Transverse Flow. *J. Fluid Mech.* **178**, 119–136.

Le Bret, M. & Zimm, B. H. 1984 Monte-Carlo determination of the distribution of ions about a cylindrical polyelectrolyte. *Biopolymers* **23**, 271–285.

Levine, S., Levine, M., Sharp, K. A. & Brooks, D. E. 1983 Theory of the electrokinetic behaviour of human erythrocytes. *Biophys. J.* **42**, 127–135.

Luft, J. H. 1965 Fine structure of capillary and endocapillary layer as revealed by ruthenium red. *Proc. Fed. Am. Soc. Exp. Biol.* **25**, 1773–1783.

Marcus, R. A. 1955 Calculation of thermodynamic properties of polyelectrolytes. *J. Chem. Phys.* **23**, 1057–1068.

https://doi.org/10.1017/S0022112098004030 Published online by Cambridge University Press

Matthews, M. B. 1975 *Connective Tissue: Macromolecular Structure and Evolution.* Springer.

Mestel, A. J., Mokady, A. J., Parker, K. H. & Winlove, C. P. 1999 Effects of the glycocalyx on the electrophoretic mobility of red cells and on streaming potentials in blood vessels: Predictions of a structurally-based model. (Submitted to *Biorheology*.)

Pedley, T. J. 1980 *The Fluid Mechanics of Large Blood Vessels.* Cambridge University Press.

Phillips, C. G. 1987 Transport in biological tissue and in shear flow. *PhD thesis,* Cambridge University.

Russel, W. B., Saville, D. A. & Schowalter, W. R. 1989 *Colloidal Dispersions.* Cambridge University Press.

Sangani, A. S. & Acrivos, A. 1982 Slow flow past periodic arrays of cylinders with. application to heat transfer. *Intl J. Multiphase Flow* **8**, 193–206.

Sawyer, P. N. & Srinivasan, S. 1972 The role of electrochemical surface properties in thrombosis at vascular interfaces: cumulative experience of studies in animals and men. *Bull. NY Acad. Med.* **48**, 235.

Seaman, G. V. F. 1983 The electrochemical properties of the peripheral zone of erythrocytes. *Ann. NY Acad. Sci.* **416**, 176–189.

Sherwood, J. D. 1980 The primary electroviscous effect in a suspension of spheres. *J. Fluid Mech.* **101**, 609–629.

Sherwood, J. D. 1981 The primary electroviscous effect in a suspension of rods. *J. Fluid Mech.* **111**, 347–366.

Sparrow, E. M. & Loeffler, A. L. 1959 Longitudinal laminar flow between cylinders arranged in a regular array. *AIChE J.* **5**, 325–330.

Tsay, R.-Y. & Weinbaum, S. 1991 Viscous flow in a channel with periodic cross-bridging fibres: exact solutions and Brinkman approximation. *J. Fluid Mech.* **226**, 125–148.

https://doi.org/10.1017/S0022112098004030 Published online by Cambridge University Press